This item is the archived peer-reviewed author-version of:

Three-dimensional modeling of energy transport in a gliding arc discharge in argon

Three-dimensional modelling of energy transport in a gliding arc discharge in argon

St Kolev[1,3], A Bogaerts[2]

[1]Faculty of Physics, Sofia University, 5 James Bourchier Boulevard, 1164 Sofia, Bulgaria

[2]Research group PLASMANT, Department of Chemistry, University of Antwerp, Universiteitsplein 1, B-2610 Antwerp, Belgium

[3] Author to whom any correspondence should be addressed

E-mail: skolev@phys.uni-sofia.bg and annemie.bogaerts@uantwerpen.be

Abstract

In this work we study the energy transport in a gliding arc discharge with two diverging flat electrodes in argon gas at atmospheric pressure. The discharge is ignited at the shortest electrode gap and it is pushed downstream by a forced gas flow. The considered current values are relatively low and therefore a non-equilibrium plasma is produced. We consider two cases, i.e., with high and low discharge current – 28 mA and 2.8 mA, and a constant gas flow of 10 L/min which has a significant turbulent component of the velocity. The study presents an analysis of the various energy transport mechanisms responsible for the redistribution of the Joule heating to the plasma species and the moving background gas. The objective of this work is to provide a general understanding of the role of the different energy transport mechanisms on the arc formation and sustainment, which can be used for the improvement of existing or new discharge designs. The work is based on a 3D numerical model, combining a fluid plasma model, the Shear Stress Transport Reynolds Averaged Navier-Stokes (SST RANS) turbulent gas flow model and a model for gas thermal balance.

The obtained results show that at higher current, the discharge is constricted within a thin plasma column with several hundred of Kelvins above room temperature, while in the low current discharge, the combination of intense convective cooling and low Joule heating prevents discharge contraction and the plasma column evolves to a static non-moving diffusive plasma, continuously cooled by the flowing gas. As a result, the energy transport in the two cases is determined by different mechanisms. At higher current and constricted plasma column, the plasma column is cooled mainly by turbulent transport, while at low current and unconstricted plasma, the major cooling mechanism is energy transport due to non-turbulent gas convection. In general, the study also demonstrates the importance of turbulent energy transport in redistributing the Joule heating in the arc and its significant role for the arc cooling and the formation of the gas temperature profile. In general, the turbulent energy transport lowers the average gas temperature in the arc and thus it allows additional control of thermal non-equilibrium in the discharge.

1. Introduction

Gliding arc discharges (GADs) are DC or low frequency AC discharges produced between two electrodes [1,2]. In the classical configuration, the electrodes are flat and diverging from each other. The plasma channel moves along the electrodes due to a forced gas flow and when its length reaches a critical value, the discharge diminishes and it reignites at the shortest electrode gap. Besides this classical configuration, there are several other designs, addressing the need of specific optimization for specific applications, like for example discharges with multiple electrodes [3,4], a magnetically stabilized gliding arc (MGA) reactor [5], a reactor with vortex gas flow [6,7], etc. The GAD is very promising for various applications, such as CO_2 conversion [7,8], dry reforming of methane [9,10], N_2 fixation [11,12], surface treatment [13] and even waste treatment [14]. This type of discharge is attractive, because it allows the generation of relatively dense plasma in the order 10^{20}-10^{22} m^{-3} while sustaining a relatively low gas temperature below 2000-3000 K. Taking into account that the electron temperature in these discharges is in the order of 1-2 eV, it is clear that GADs produce thermally non-equilibrium plasmas, which are found to be preferable for various plasma assisted gas conversion processes [1].

The thermal non-equilibrium behavior of GADs is related to several characteristics, like their nonstationary cyclic nature, the forced gas flow, the electrode configuration and the power supply parameters. It is rather difficult to generalize the contribution of the different energy transport mechanisms, due to the large variety of discharge configurations, working gases and applied electrical power. In all cases, however, the degree of non-equilibrium is the result of a balance between heating and cooling of the background gas. To our knowledge, the problem of energy transport in GADs was only partially discussed in literature. Discussions about it can be found in several earlier works [15-17] and in more recent papers [18-22].

In this work, we present a more systematic analysis of the cooling mechanisms and the energy balance in the GAD with a typical two-electrode configuration in argon gas. The aim of this study is to analyze the contribution of the various energy transport mechanisms and to provide a general understanding of their role in the discharge sustainment and formation. In general, we seek for conditions which favor a higher degree of thermal non-equilibrium and gas temperature in the order of several hundred degrees Celsius. Even lower gas temperature values might be of interest in some applications where temperature sensitive materials are treated.

Although the results in this study are obtained for a limited number of different discharge conditions like electrical current, gas flow and gas type, the discharge conditions are chosen so that the obtained behavior is representative for the possible discharge regimes in low current arcs in different gases and electrode configurations. The study is based on 3D numerical modelling of the discharge, including a coupled plasma, gas and electrical circuit description. This work can be considered as an extension of the above mentioned studies [18-21]. More specifically, the model extends the previous work in several directions: 1) It uses a 3D, fully coupled plasma-gas model, which is capable of providing a more complete view of the discharge physics and quantitatively more correct results. Previous studies were mainly focused on the general discharge behavior and most of them were based on 2D models, which allows for qualitative characterization of the discharge. 2) It provides a quantitative measure of the relative importance of the different energy transport mechanisms, which was not studied before. 3) It provides quantitative results for the effect of the plasma on the gas flow, which was previously ignored (except in [18]). 4) Finally, it provides an analysis of the role of turbulent transport on the discharge formation.

The paper has the following structure: In section 2 we briefly describe the model developed for the GAD description. The obtained results are presented in section 3. In subsection 3.1 we give a general overview of the plasma and gas characteristics for two cases with different discharge current. Subsection 3.2 is devoted to the thermal balance of the discharge and the energy transport mechanisms. Finally, a conclusion is given in section 4.

2. Model description

The numerical model used here is a 3D model and considers the geometry of figure 1, showing a discharge cross section. The geometry corresponds to an experimental set-up described in [24,25] and it includes two simple knife-shaped electrodes with diverging distance between them and an gas inlet nozzle below. The shortest distance between the electrodes is 3.2 mm. The discharge is powered by a simple external discharge circuit, including a DC voltage source with a voltage of 3700V and a current limiting resistor in series. The resistor value is 132 kΩ for the case of 28 mA discharge current and 1.32 MΩ for the 2.8 mA discharge current.

Below we provide a brief description of the model and its implementation; more details are given in Appendix A. The model is based on a previously developed plasma model, which in this work is fully coupled in time to a gas flow description, based on the Shear Stress Transport Reynolds Averaged Navier-Stokes (SST RANS) turbulent model [26] and gas thermal balance. The geometry includes two domains, used in two consecutive stages of the simulations. The division in two domains is implemented in order to reduce the computation time during the discharge simulation, by excluding part of the domain which does not change due to the presence of plasma.

During the **first stage**, only the SST turbulent gas flow model is solved in the whole domain "A", assuming that there is no plasma and thus no gas heating. The gas inlet is a small nozzle with diameter of 1.5 mm and the applied gas flow rate is 10 L/min at atmospheric pressure. The electrodes and the outer wall have no slip boundary condition, the gas inlet (the nozzle) has a fixed normal velocity of 95 m/s and at the gas outlet, the boundary condition is fixed at atmospheric pressure. The model is solved until steady state is reached. Thus, in this way we obtain an accurate and realistic solution of the gas flow, including the effects related with the nozzle.

Figure 1. Cross section of the geometry considered in the numerical model. The arc in different moments in time is represented schematically with orange lines.
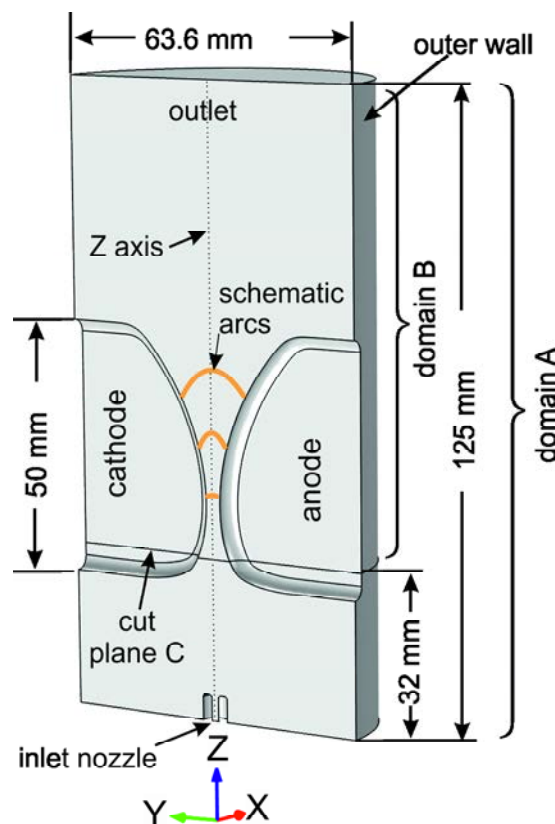
During the **second stage**, all equations of the model are solved simultaneously, but in a somewhat reduced domain B. The domain is obtained from domain A by removing the part below cut plane C (see figure 1), i.e. the plane C appears as a gas inlet boundary for the domain "B". This is done in order to avoid the calculation of the equations related to the plasma species and electric field in the whole domain and instead to solve them only in a reduced region in which the plasma can have a certain influence on the flowing gas. One can go even further and reduce the domain in the radial direction as well, but this was not done in the current implementation of the model.

The system of equations includes the SST gas flow model [26, 27], the plasma model and the model for gas thermal balance. The plasma model is based on the fluid approach and it considers the following species: electrons, Ar^+ argon ions, Ar_2^+ argon molecular ions and $Ar(4s)$, which represents all 4s levels, considered as a single lumped excitation level. The plasma model is based on the assumption of plasma quasi-neutrality and ignores the wall plasma sheaths. The model includes the electron energy balance equation, a simplified form of the current conservation equation and the balance equations of the considered species Ar^+, Ar_2^+, and $Ar(4s)$, while the electron density is simply obtained as the sum of the positive ion densities. The excited atoms Ar(4p) and molecules Ar_2* are also taken into account in an effective way (see the appendix). The electric field due to the external field affects the plasma only as a Joule heating term in the electron energy equation and does not enter in the particle fluxes. The latter take into account only the ambipolar field calculated based on equality of fluxes of positive and negative species. The boundary conditions for the species densities and the electron energy are defined by a zero gradient on all boundaries, i.e. there are no particle and electron energy losses at the walls, but they are lost at the gas outlet due to convective transport. With respect to the gas thermal balance equation, the boundary condition is again a zero gradient of the gas temperature, except at the cut plane C, where the gas temperature is fixed at $T_{g0} = 293.15$ K, which is also the initial gas temperature in the whole domain.. In [20,21] more discussions about the model validation and limitations can be found.

The gas flow model in the second stage of the simulation is the same as in the first stage, with minor adjustment due to the domain change. The simulation starts with initial values for all variables, taken from the gas flow solution obtained at stage 1. While these variables might change in the domain during the time stepping of the simulation at stage 2, the values of the velocity, pressure and the turbulent variables at the cut plane C are assumed to remain constant, since they appear as a gas inlet boundary condition for the gas flow model in stage 2.

The plasma column is initiated by imposing a heating term in the electron energy balance equation, confined within a small region at the position of the shortest electrode gap (z = 0.016 m), with relatively low value so that the produced electron density in the order of 10^{18} m^{-3} is much lower compared to the density value in the fully developed arc sustained by the discharge current. The latter is usually in the order of 10^{20} m^{-3}. This initial heating is applied for a time shorter than 10 μs.

The model is implemented within Comsol Multiphysics 5.2 software. Because the plasma sheaths are neglected in the model, the obtained results will not change if we exchange the electrodes or if we switch the voltage source polarity. Therefore, there are two planes of symmetry in the considered geometry (see figure 1) – i) the YZ plane in the middle of the electrodes (x=0) and ii) the XZ plane between the electrodes. Thus, in the final model only ¼ of the whole domain is solved, to save calculation time, assuming symmetry boundary conditions for the boundaries lying on the XZ and YZ planes.

3. Results and discussion

3.1. General discharge behavior

3.1.1 Discharge current I_d = 28 mA

In this subsection we present the major discharge characteristics, so that we can place the later discussion about the energy transport in the context of these data. As noted before, the initial gas velocity, before the discharge ignition, is calculated in the whole domain, including the gas nozzle (see figure 1). Figure 2 illustrates the initial (undisturbed by plasma) distribution of the gas velocity, both in the YZ plane (left side) and the XZ plane (right side). When the discharge is ignited and the discharge evolves in time, the gas velocity remains approximately the same as the velocity without plasma. Hence, the gas velocity distribution at later times within the discharge looks very similar to what is shown in figure 2, although the plasma heating and thus the gas expansion causes some minor perturbations (below 5%) in the gas velocity around the arc. This is visualized in figure 3, presenting a zoom of the velocity variation along the Z axis at different moments in time, only in the region around the arc initiation $z \in (1.5 - 2.2 \text{ cm})$. In the other regions, at 2-3 mm away from the arc, the gas velocity perturbation due to the arc remains small and less than 1%, i.e. in practice the velocity is equal to the undisturbed solution.
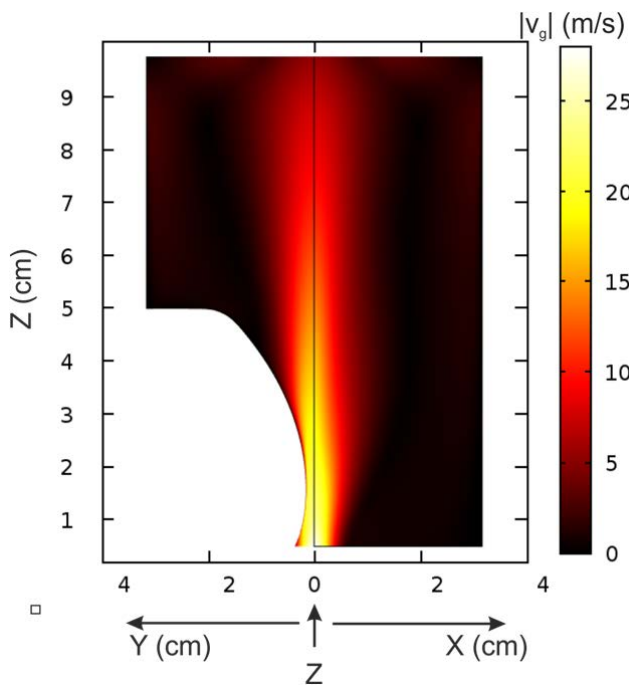

Figure 2. Initial gas velocity distribution, undisturbed by plasma, used as initial condition for both discharge current cases - 28 mA and 2.8 mA. The left side of the figure shows the YZ plane (x=0) and the right side shows the XZ plane (y=0). The electrodes lie in the YZ plane (see figure 1).
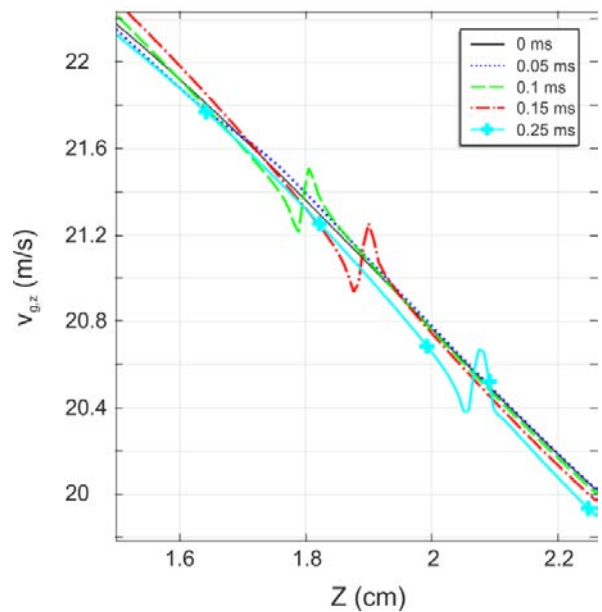
Figure 3. Zoom of the gas velocity distribution along the Z axis around the positions of the arc for different moments in time. The figure shows the perturbations in the gas velocity caused by the arc heating. The discharge current is 28 mA. The undisturbed initial distribution of the gas velocity corresponds to time = 0 s.

As a result of the small nozzle diameter and the significant gas flow rate (10 L/min), the gas flow remains rather confined around the central Z axis, as is obvious from figure 2. The velocity magnitude at the shortest gap position (z = 16 mm), where the arc is initiated, is in the order of 22 m/s (see figure 3).

Figure 4 shows contour plots of the gas temperature and the electron density for the higher current case (28 mA). We clearly see a difference in the evolution of both variables. The cross section of the electron density distribution remains approximately the same in time and only minor changes can be observed, i.e. the diameter of the plasma column, the current channel and the Joule heating remain almost constant in time, while this is not the case for the T_g profiles. Indeed, the energy transport from the plasma column towards colder regions leads to

widening of the T_g distribution in time. The difference can also be easily seen from the 1D distribution along the Z axis, shown in figure 5. The widening of this warm region means that the volume where the temperature is above a certain value increases.
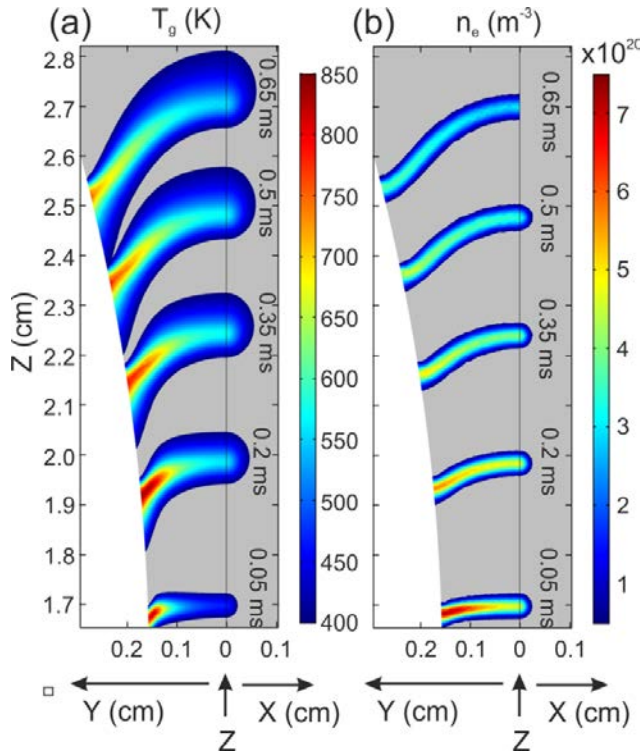

Figure 4. (a) Gas temperature (T_g) and (b) electron density (n_e) distribution in the YZ plane (left side of the figures) and in the XZ plane (right side of the figures), at different moments in time, as indicated in the figures. Discharge current I_d = 28 mA. The discharge voltage is 216 V at 0.65 ms (excluding the wall sheaths).
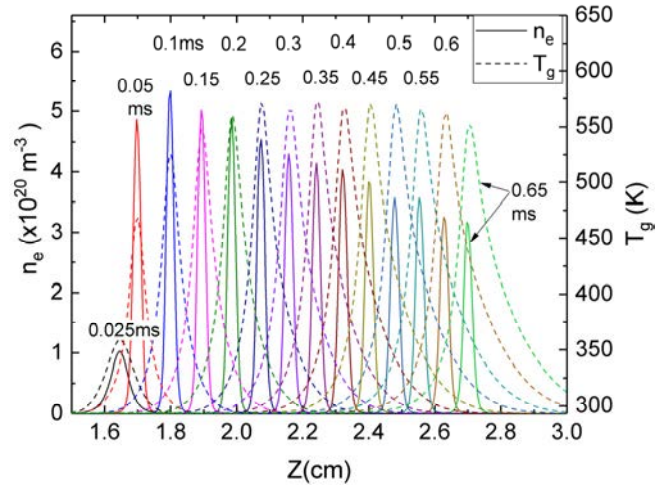
Figure 5. Gas temperature (dashed lines) and electron density (solid lines) distribution along the Z axis, at different moments in time, as noted in the figure expressed in milliseconds. Discharge current I_d = 28 mA.
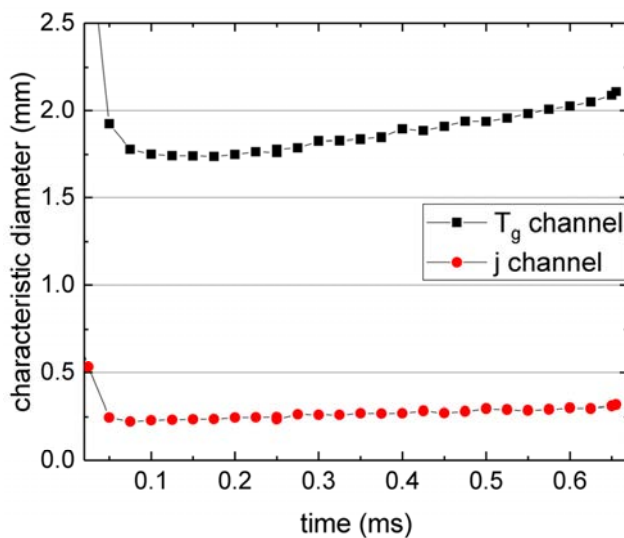

Figure 6. Characteristic diameter of the current density channel and the T_g channel. I_d = 28 mA.

If we define, however, a characteristic diameter of the T_g and current density j (proportional to n_e) variation in the XZ plane as $d_{T_g \text{ or } j} = 2\sqrt{\dfrac{\int (T_g \text{ or } j)\mathrm{d}\Omega}{\pi \max(T_g \text{ or } j)}}$ and plot it (figure 6), we actually observe a very slight variation of both diameters. This means that the visual increase of the warm region (figure 4) is mainly due to the increase of the peak T_g value and not due to changes in the shape of the T_g distribution. The drop of the diameter at the beginning in figure 6 corresponds to the discharge initiation, when the plasma column is not constricted.

Figure 5 also shows another trend – while the peak T_g initially slightly rises in time and the profile widens, the electron density decreases. This is related to the slight increase in diameter of the current density channel which, although hardly visible in figure 6, increases with around 12% between 0.1 ms and 0.25 ms. Note that around 0.25 ms, T_g stops rising and converges towards a constant value, as also shown in experimental measurements [24,25]. At later times (0.6 ms) the gas temperature even starts to slowly decrease.
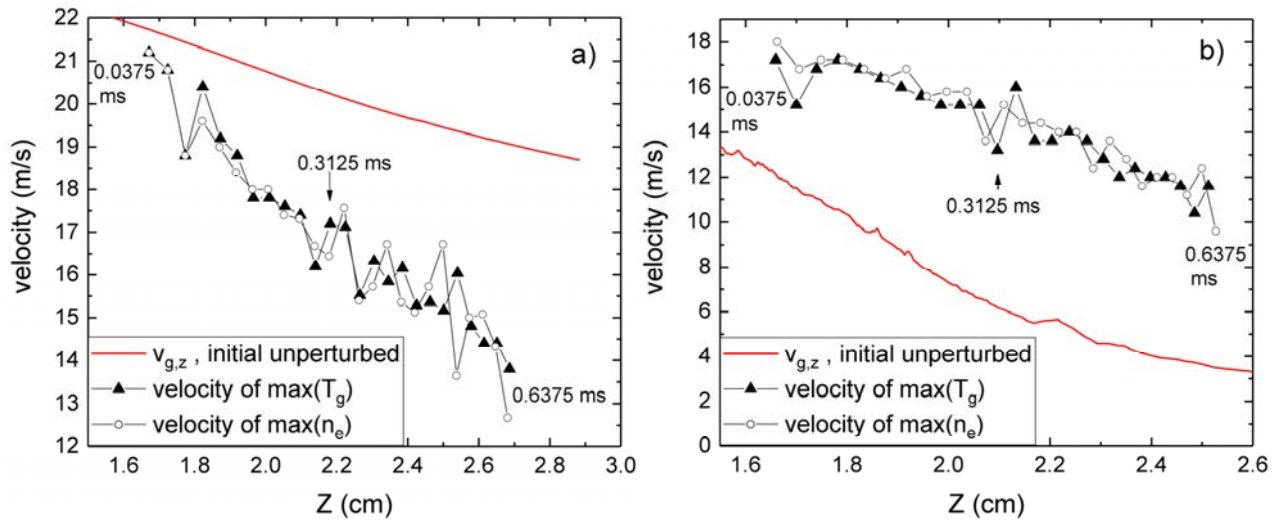

Figure 7. Displacement velocity of the maximum values of T_g (triangles) and n_e (open circles) along (a) the Z axis and (b) at a distance of 0.1 mm from the electrode. The undisturbed (and initial) gas velocity distributions are also shown for comparison (red line). I_d = 28 mA.

In figure 5 one could also notice that after 0.25 ms, there is a slight displacement between the n_e and T_g profile – the n_e profile lags behind T_g. This is attributed to another more significant lag, namely the plasma channel moves with slower velocity compared to the gas velocity and the plasma column slips with respect to the gas. Figure 7(a) shows three different velocities along the Z axis, i.e., 1) the undisturbed z component of the gas velocity ($v_{g,z}$), which approximately coincides with the actual gas velocity profile in every moment, with minor variations of the gas velocity due to the plasma perturbations as shown in figure 3; 2) the velocity of the T_g peak value and 3) the velocity of the n_e peak value. Apparently, the plasma column is slower than the gas, with a relative slip velocity generally rising with time (or distance travelled) and reaching 5 m/s at 0.65 ms. This phenomenon has been observed also in several experimental studies [28,29]. The main reason for the observed slip in our model is the asymmetry of the electric field with respect to the plasma column which, for the considered geometry, consists of increased electric field below the plasma column at the Z axis. As a result, the plasma column migrates towards the higher electric field regions, while the gas pushes it towards the lower electric field regions. The asymmetry of the electric field is caused by two effects: i) the shape of the diverging electrodes leads to an increasing distance between them along the Z axis (upwards or downstream; see figure 1). Thus, for a given voltage, the electric field increases downwards, with a maximum at the position of the shortest electrode gap. ii) The bending of the plasma column causes an increasing electric field when the angle becomes smaller than 180 deg, i.e. when it is bended. The bending itself is caused mainly by the inhomogeneity in the gas flow velocity, which forces the different parts of the plasma column to move with different velocity, resulting in bending and stretching. By stretching we simply mean the elongation of the arc

length with time as a result of the higher velocity in the discharge center (the Z axis) with respect to the electrodes, and moreover due to the diverging geometry of the electrodes. Additional irregularities in the arc shape caused by gas turbulences may also contribute to the arc bending and stretching, but they are not considered in our model since the gas description is based on averaging the effect of turbulences (RANS model). Note also that the sharp variations of the velocities of $\max(T_g)$ and $\max(n_e)$ in figure 7 (for example at $z = 1.8$ cm) are not a physical phenomenon but a numerical artefact. The spatial discretization of the domain (the mesh) needed for the numerical solution of the equations, forces the maxima to appear at the nodes of the mesh and thus the displacement of the maxima is not smooth but "jumping" from node to node. The latter leads to these unphysical variations of the obtained velocities. A finer mesh would reduce these effects, but it would increase the computation time several times, i.e. up to months, and would not affect the general results and general message.

It should be noted that while at the center (along the Z axis) the plasma column lags behind the gas flow, near the electrode surface it is the opposite. This effect is clearly visible from figure 7(b) which shows the displacement velocity of T_g and n_e at a distance of 0.1 mm from the electrode, i.e. roughly at the position where the gas flow wall layer starts. The gas velocity is zero at the electrode surface while the rest of the plasma column moves and thus the plasma column tends to bend there. This forces the plasma to "glide" on the electrode surface – the electron density outpaces the gas velocity and the gas temperature in the vicinity of the electrode surface. The latter is also apparent from figure 4, where the displacement between the maxima of T_g and n_e near the electrode is significant. The effects of bending on the relative velocity were also briefly discussed in [23] and in more detail in [30].

Thus, at 28 mA current, the lag in n_e peak along the Z axis is mainly related with the electric field inhomogeneity due to the electrode shape, while at the electrode surface, the bending of the plasma column is mainly responsible for the difference in the gas, n_e and T_g velocities. Note that at later stages of the time evolution, the plasma column might become strongly bended in the center and thus the bending might become the major reason for the slip velocity in the center as well.

Note also that we do not consider here the back-breakdown (BB) process [20,28] characterized by rapid, jump-like displacement of the plasma channel or only part of it, which leads to an effective slip between the plasma and the gas. In [20] it was shown that the BB process might have significant effect on the "gas cooling". Indeed, the maximum gas temperature of the arc in the part subject to back-breakdown was reduced with about 20-30%. It is rather difficult to estimate the exact contribution of this process as an effective energy transport mechanism since its appearance is often related to irregularities in the arc shape, controlled by stochastic processes like turbulent gas flow. Therefore, in [31] the effect was simulated as being dependent on the event frequency considered as an external parameter. In section 3.2 we will compare the effect of the BB process with the other energy transport mechanisms based on a simple estimation of its contribution.

3.1.2 Discharge current I_d = 2.8 mA

Figure 8 illustrates the distribution of T_g and n_e for the lower current of 2.8 mA. The results are obviously very different from the 28 mA case (figure 4). First of all, the gas temperature rises only slightly (20-30 K) above the background temperature. This slight increase in T_g does not allow the contraction of the plasma column. Note that it is assumed in the model that the initial gas breakdown appears in a tiny channel and thus we initially induce (in the first 10 μs) a relatively tiny channel with diameter of around 1 mm with low density plasma, i.e. we basically enforce the initial channel to be partially constricted. Despite that, the distributions in n_e and thus also in the current density j and the Joule heating Q_E gradually widen in time (see figure 8(b) for n_e). Indeed, at 0.4 ms we observe a very diffusive distribution, typical for a low pressure glow discharge. Although in the model we do not describe the wall sheaths, at this low current value and cold cathode conditions, we expect that the plasma-electrode attachment will be like for a glow discharge – secondary electron emission. This is because the current value is very low and thus it cannot sustain neither thermal electron emission nor field emission from the cathode. Thus, a wide spot with

current density determined by secondary electron emission from the cathode is expected at these conditions, as it was observed in [32, 33].
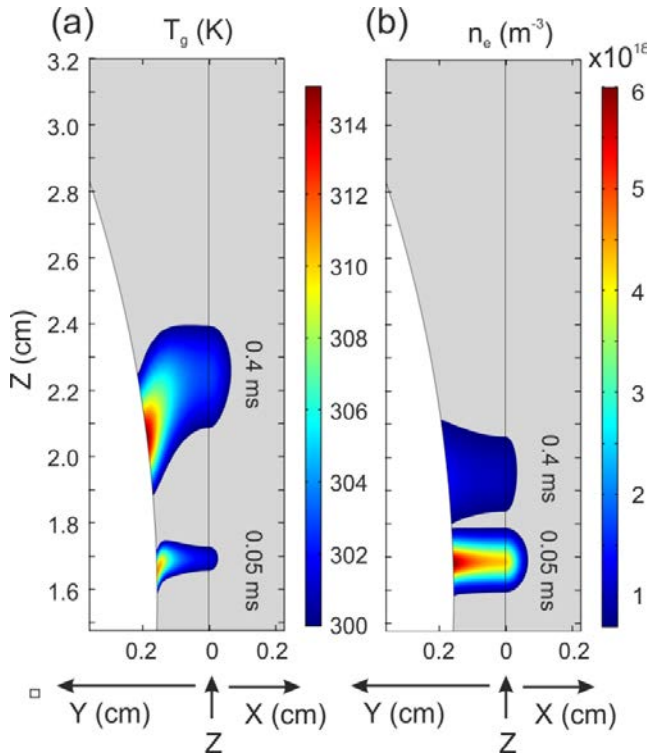

Figure 8. (a) Gas temperature (T_g) and (b) electron density (n_e) distribution in the YZ plane (left side of the figures) and in the XZ plane (right side of the figures), at two different moments in time, as indicated in the figures. Discharge current $I_d = 2.8$ mA.
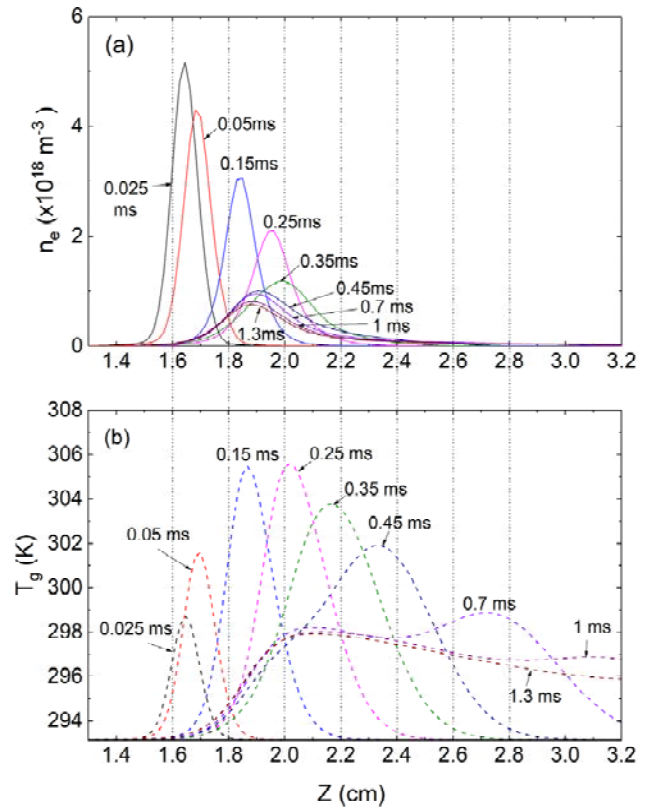

Figure 9. (a) Electron density and (b) gas temperature distributions along the Z axis, at different moments in time, as noted in the figure. Discharge current $I_d = 2.8$ mA.

Another important feature of the 2.8 mA case is that the n_e and j distribution do not follow the gas flow. This can be seen in figure 9(a). Initially, since the plasma column is relatively compact and exhibits a certain increase in T_g, n_e and j partially follow the gas flow, and the plasma channel is pushed downstream (upwards in figure 8 and to the right in figure 9). Later, the plasma column becomes very wide and the current density very low, which results in T_g being only a few K above the background value (see figure 9(b)). At that stage, there is no constriction of the plasma column and thus the n_e profile is not determined by the hot gas region, but it is determined mainly by the electric field distribution and the convective transport of the heavy plasma species. Therefore, at around 0.32 ms, the maximum value of the n_e profile stops moving downstream and starts moving backwards (towards lower Z values). The T_g maximum value continues moving downstream, but we should stress that this slightly hotter gas is heated by the plasma at earlier times when it had higher current density. After 0.6 ms the plasma stabilizes slightly above the shortest gap position and the plasma parameters vary only slightly in time, evolving towards a stationary glow discharge reached at about 1.3 ms. Figures 9 and 10 show that the steady state maximum n_e value is at Z = 1.88 cm, i.e. around 2.8 mm above the initial breakdown position (Z = 1.6 cm) and the maximum of T_g is slightly shifted towards higher Z values. Thus, at steady-state, we can no longer talk about "gliding arc discharge" but this is a diffusive glow discharge between two electrodes.

Note that in general, if there is no additional force pushing the charged and excited particles in a certain direction, they will follow the gas flow and thus the plasma will move with the gas flow velocity. The reason for that is simply the fact that the charged particles are born with a directed collective velocity component, being the gas velocity. Thus if we hypothetically consider a discharge between parallel plates and ignore the possibility of arc

attachment to particular points on the electrode, the arc (plasma) should follow the gas motion. Actually if we ignore the gas heating and any possible instabilities related to the electric field, ideally the discharge is expected to evolve to a homogeneous discharge. In the low current GAD at 2.8mA considered here, although there is no significant gas temperature, the plasma does not follow the gas since the produced electric field is inhomogeneous and it produces more plasma in the regions with lower gap distance. The produced plasma moves with the gas downstream, but when the electric field decreases significantly due to the increasing interelectrode distance, the plasma quickly decays due to the recombination processes.

In the case of higher current (28 mA), the higher gas temperature in the arc center leads to reduction of the gas density and thus it facilitates the gas ionization and reduces the electron energy losses for elastic collisions. As a result, the hotter region provides a low resistance path and therefore the electric current follows this channel. The large difference in the plasma resistance is also found in the results obtained here - in figure 8 (28 mA, t = 0.65 ms) the discharge voltage is 216 V, while for the lower current case in figure 10, for 2.8 mA the voltage is 195 V. Obviously, the resistance in the latter case is almost 10 times higher (195V/2.8mA versus 216V/28mA) despite the shorter length of the plasma channel - figure 10(b) vs figure 4(b) at 0.65 ms.

Here we should open a short discussion on the obtained results and the limitations of the model. While the diffusive nature of the plasma column at so low current values is indeed most probable for the considered discharge conditions [32], we should remind the lack of plasma sheaths in the model, and thus the plasma-cathode attachment is not accounted for in the model. In close vicinity to the cathode, the plasma channel will be constricted in a cathode spot, which is typical for the glow regime. Based on [32-34] we expect the diameter of the spot to be in the order of 1 mm or less, which is smaller than what we see in figure 8(b) at 0.4 ms, where the attachment region to the electrode extends within 2-3 mm. Thus the results obtained here for the plasma parameters near the electrodes should be considered to be valid only at a distance 0.1-0.2 mm from the cathode surface, which is typically the distance over which the near-electrode plasma structure does not affect the plasma column [32, 34]
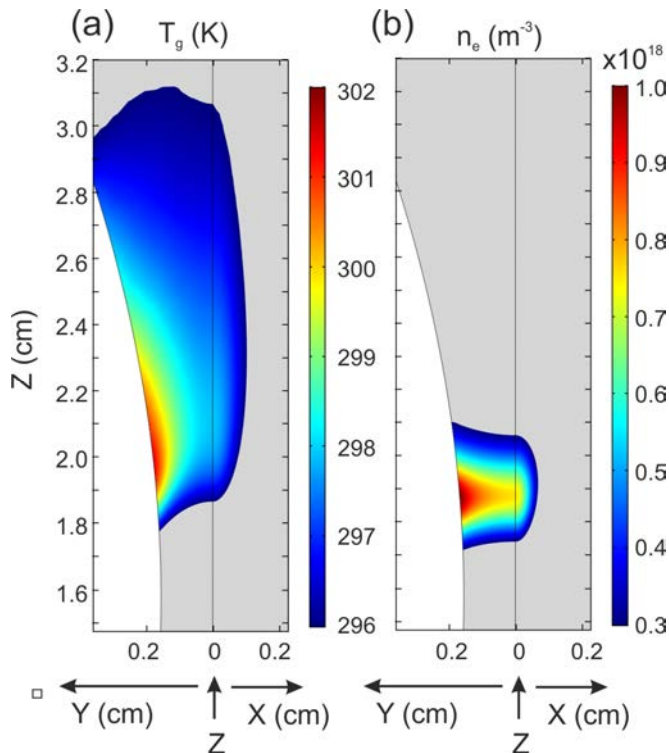

Figure 10. Steady-state solution for the (a) gas temperature (T_g) and (b) electron density (n_e) distributions in the YZ plane (left side of the figures) and in the XZ plane (right side of the figures. Discharge current I_d = 2.8 mA, discharge voltage 195 V.

It is clear from the above analysis that the lower and higher current regimes pose rather different properties. Experimental studies [33,35] show that the transition between the two regimes is not smooth but rather abrupt. Note that the transition from diffusive to contracted discharge will take place at higher current values if the gas cooling mechanisms are intensified (for example at higher gas flow) and vice versa. Moreover, the exact value of the transition current might be different, depending on whether we change the current starting from low or from high current, i.e. there might be a hysteresis in the current-voltage characteristic, as observed in [33,35]. In some cases [33], the existence of such hysteresis is accompanied with unstable discharge in this region of the current-voltage characteristic, which is expected keeping in mind that for given current value in the hysteresis region, there are two points of operation with two voltage values. In addition, for different gas types or mixtures and different gas cooling conditions, the transition will also take place at different current values. In [8] for example, in CO_2 and significant gas flow, two distinct low and high current regimes were observed below 50 mA and above 250 mA with unstable discharge in between. We should also note that the I-V characteristic will have one more sharp variation (transition) at a point where the cathode plasma region transits from secondary electron emission to field or thermo-field electron emission. The transition is accompanied with a sharp voltage drop. The transition process between the two regimes is out of the scope of this study, but we expect our conclusions to be valid in the region of transition as far as the discharge is stable for long time. The energy transport mechanisms might be affected in the transition region, if the discharge is highly unstable and transits from one mode to the other in short time. We do not expect any qualitative difference in the discharge operation and thus we have not simulated a discharge with intermediate current values. Moreover, due to the complexity of the transition and its threshold nature, we expect that the exact values of the transition currents will be highly susceptible to uncertainties in the model input data, assumptions and boundary conditions.

With respect to applications, it is rather difficult to make generalizations for the use of the different discharge regimes. The diffusive, low current regime of the discharge provides cold gas operation, which might be desirable for certain applications. In addition, in this regime it is rather easy to control the treated gas, since the plasma is stationary and we can force the gas to pass through the active zone. On the other hand, if the desired process depends non-linearly on the electron density and if high n_e is required for better efficiency, the constricted discharge mode will be preferable. However, in this regime, the arc more or less follows the gas flow and does not treat a significant amount of gas.

3.2. Energy transport for arc cooling

In this section we focus on the energy transport from the hot gas within the plasma column towards the cold surrounding gas. However, before doing that, we need to briefly discuss the electrical energy deposition into the various components of the plasma and its conversion to gas heating. Due to the large mass ratio between positive ions and electrons, the electric field mainly heats the electrons. Due to the atmospheric pressure operation, we assume in the model that the electron energy losses are due to energy fluxes and collisions, with the latter significantly prevailing (above 99%), i.e. ensuring a locality of the energy deposition from the electrons to the neutral argon atoms. For the considered conditions of an atmospheric pressure argon plasma, around 90% of the energy is directly transferred to the neutral gas by elastic collisions, while the remaining energy is spent for inelastic collisions, mainly excitations. This significance of elastic collision energy losses is expected, since only high energy electrons are capable to excite the electronic states of the argon atoms (lowest excitation energy = 11.55 eV) and the concentration of argon dimers and ions is too small to have some influence. Furthermore, we assume pure argon with no impurities. Note that a significant part of the energy spent for inelastic collisions is finally deposited to the neutral gas and as the model solutions show, only a small part (below 2%) is emitted as light. Therefore, it is relatively safe to assume that all the energy is transferred to the background gas, and thus its redistribution out of the energy deposition region, where the current density and thus Joule heating are significant, determines the gas temperature in the plasma channel. In this section we identify the possible mechanisms of energy transport, providing cooling of the neutral gas in the plasma channel and thus controlling the rate of thermal non-equilibrium. The latter is important for various applications. For example, in plasma assisted CO_2 decomposition, a lower gas temperature is desirable to achieve a high energy efficiency and conversion rates [30,31,37,38]. Indeed, the plasma produced by GADs is actually often too close to thermal equilibrium, due to the considerable gas temperature, so that vibrational levels are depopulated by vibrational-translational (VT) relaxation. As a consequence, there is no (significant) overpopulation of the higher vibrational levels in the vibrational distribution function (VDF), i.e., the VDF is too close to thermal equilibrium. If the VDF could be more overpopulated in the higher levels, the energy efficiency of CO_2 conversion could be further enhanced. Although this study is in argon gas, it is still relevant to other gases including CO_2 since it provides results for the general discharge behavior and the conclusions made here can be easily transferred qualitatively to other gases. We expect similar behavior to be present in CO_2, air etc. but for different ratios of the major discharge characteristics, like electric current, gas flow and turbulent transport. Therefore, the analysis given in this work provides better understanding of the mechanisms of gas cooling and energy transport, which can give directions for optimizations of GADs in different gases.
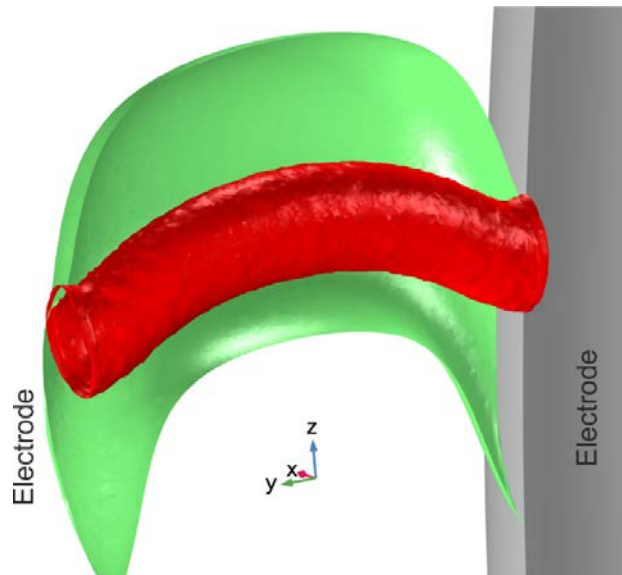

Figure 11. Isosurfaces used for the determination of the energy transport. The red surface $\Omega_{95\%P}$ surrounds a domain in which 95% of the power is deposited (isosurface $Q_E = 1.5\times10^8$ W/m^3). The green surface $\Omega_{50\%Eth}$ surrounds the domain containing 50% of the internal thermal energy in the gas (isosurface $T_g = 336$ K). The left electrode is not shown for better visualization of the isosurfaces. Conditions: $I_d = 28$ mA at 0.25 ms.

For the energy transport analysis, we need to study the energy fluxes in and out of a certain domain, i.e. normal to its surface. Here we define two domains:

a) a domain $\Omega_{95\%P}$ in which 95% of the total discharge power P is deposited. In practice this corresponds to the power density Q_E exceeding a threshold value $Q_{E,th}$, which is derived from the condition:

$$\int Q_E(Q_E > Q_{E,th})d\Omega = 0.95P \tag{1}$$

This domain corresponds to the power deposition and it will be used when we discuss how Joule heating is redistributed. In the text we will use the term "plasma column", which corresponds in principle to the region where most of the charged particles are found, but since the Joule heating is tightly connected to the electron density, in practice the "plasma column" coincides with the $\Omega_{95\%P}$.

b) a domain $\Omega_{50\%Eth}$ containing 50% of the total internal thermal energy E_{th} in the gas, assumed to be equal to the sensible energy. E_{th} is calculated based on the gas temperature relatively to the background (initial) temperature T_{g0} = 293.15 K i.e. based on (T_g - T_{g0}). We use the following expression for the specific internal sensible energy E_{int} [40]:

$$E_{int} = \int_{T_{g0}}^{T_g} C_p dT_g - p_g/\rho_g \tag{2}$$

Where C_p is the specific heat capacity at constant pressure, p_g and ρ_g are the gas pressure and mass density, respectively. In practice we define this domain as a region where T_g exceed a threshold value $T_{g,th}$ defined by the equation:

$$\int \rho_g E_{int}(T_g > T_{g,th})d\Omega = 0.5 * \int \rho_g E_{int}d\Omega = 0.5 * E_{th} \tag{3}$$

The use of this additional domain is motivated by the fact that the gas temperature profile extends much further compared to the electron and current densities (see figures 4 and 8). Since the efficiency of energy transport from the first domain $\Omega_{95\%P}$ depends also on the gas temperature outside, it is instructive to find out how the energy is redistributed there and whether the mechanisms change.

Figure 11 illustrates these two isosurfaces, defining the above mentioned domains for the conditions of 28 mA and a time of 0.25 ms. The shape of the domain $\Omega_{95\%P}$ (red surface) is close to a bended cylinder, while the domain $\Omega_{50\%Eth}$ (green surface) is much more bended. The difference in the two domains is related to the difference in the displacement velocities of the n_e and T_g distributions discussed in the previous section, leading to a lag of the plasma column with respect to the gas velocity at the symmetry axis (in the middle of figure 11) and a lag of the gas velocity with respect to the arc at the electrode surface (near the electrodes in figure 11).

The choice of these domains is a bit arbitrary and partially subjective. The percent numbers in equations 1 and 3 are not obtained from strict mathematical or physical considerations, but they are based on simple logic and the observation that small variations of these numbers do not significantly change the conclusions made here.

We will now describe the expressions used for the calculation of the possible mechanisms for energy exchange between the hot gas in the plasma column and the environment. Usually the energy transport mechanisms are divided into 3 major categories: **radiation, conduction** and **convection** [41].

(i) Radiation energy transport is not really significant for the considered conditions of argon gas. Since this work is devoted to relatively low current arcs, far from thermal equilibrium, the typical peak gas temperatures are below 2000 - 3000 K, and therefore this energy transport remains negligible, with a contribution below a few percent. Therefore it will be ignored in the following discussions.

(ii) Conductive energy transport is related to the molecular interaction of particles with different kinetic energy, including thermal diffusion. The conductive thermal flux is calculated as $\vec{q}_d = -k_g \nabla(T_g)$, where k_g is the gas thermal conductivity. The power transferred by conduction through a surface Ω is thus $P_{d,g} = \int \vec{n}.\vec{q}_d dS$, where $\vec{n}$ is the normal vector to the surface S, surrounding the corresponding domain.

(iii) Convective energy transport is the most significant energy transport mechanism for all conditions considered here. It is related with the collective motion of species. Here we further subdivide it into the following two subcategories:

1. Convective turbulent energy transport caused by the presence of gas eddies, leading to intensive convective mass and energy transport. In the model we use a RANS based turbulent representation (SST) and thus this transport is represented as an effective conductive energy transport with effective thermal conductivity coefficient k_t, which is

added to k_g in the gas thermal balance equation, as in previous work [39]. Thus, the power transport due to turbulent gas transport is $P_{t,g} = \int -\vec{n}.k_t\nabla(T_g)dS$.

2. Convective non-turbulent energy transport, related with the bulk non-random motion of the species. We can further subdivide it into two components:

2.1) Convective energy transport in the neutral gas is assumed to be equal to $P_{a,g} = \int \rho_g E_{int}\vec{u}_g.\vec{n}\,dS$.

2.2) Convective energy transport of charged and excited species including diffusion: $P_{a,int} = \sum_i \int -E_i n_i(\vec{u}_g.\vec{n} + sign(q_i)\mu_i\vec{E}_{amb}.\vec{n}) - E_i D_i \nabla n_i.\vec{n}\,dS$, where the sum is over the type of species "i", E_i is the chemical internal energy of the given particle type (i.e. ionization energy for ions or excitation energy for the excited species), q_i is its charge, μ_i is the mobility, $\vec{E}_{amb}$ is the ambipolar electric field and D_i is the diffusion coefficient. For the excited neutral species $q_i = 0$.

Now that we have defined the various energy transport mechanisms, we will describe the energy transport from the hot gas within the plasma column towards the cold surrounding gas, for the high and low discharge current regimes.

3.2.1 Discharge current I_d = 28 mA

Figure 12 shows the most significant energy transport mechanisms for the $\Omega_{95\%P}$ and the $\Omega_{50\%Eth}$ domains, respectively. Energy transport across the $\Omega_{95\%P}$ surface (figure 12(a)) is mainly due to convective turbulent energy transport (ca. 70%), with a minor contribution from non-turbulent convective and even smaller from conductive energy transport (about 25% and 5%, respectively). Figure 12(a) also plots the values corresponding to 95% of the total power, in order to show how the energy transport due to energy fluxes compares to the deposited power. The displacement of the plasma column and the gas temperature profiles, i.e. the lag of the n_e profile behind the T_g profile as seen in figure 5, leads to a net convective non-turbulent energy transport, when calculating the integral $P_{a,g} \cong \int C_V(\rho_g T_g - \rho_{g,T_{g0}}T_{g0})\vec{u}_g.\vec{n}\,dS$ over the surrounding surface of the $\Omega_{95\%P}$ domain. For example, at the symmetry edge, on the upper side of the $\Omega_{95\%P}$ domain, T_g is higher than on the lower side. Therefore, even for constant gas velocity at the symmetry axis, the energy flux out of the domain will be higher at the upper side compared to the lower side, just because of the higher T_g. The opposite is true near the wall – the convective non-turbulent energy flux is higher at the lower side due to the higher gas temperature there.

Note also that in Figure 12 the sum of all energy transport fluxes and the 95% power deposition are not equal. In the beginning, before 0.2 ms, part of the deposited power is accumulated in the gas in the form of thermal energy due to the temperature increase, explaining why the 95% power deposition is higher than the sum of all energy transport fluxes. Later, part of this accumulated thermal energy can be released out of the domain, which leads to the slightly higher total energy transport flux compared to the 95% power deposition. In time, the domain defined by 95% of the power changes and thus it includes different amount of gas, which means also different total energy capacity. Therefore, there is no strict requirement for both curves (blue and purple) in Figure 12 to coincide at any time, unless some kind of steady state solution is reached.

For the $\Omega_{50\%Eth}$ surface (figure 12(b)), the dominant mechanism is still convective turbulent heat transport (ca. 93%), but conductive energy transport becomes relatively more significant than non-turbulent convective transport (about 5% and 2%, respectively). Actually the latter is close to zero since $P_{a,g}$ can be approximated by

$$P_{a,g} \cong \int C_V(\rho_g T_g - \rho_{g,T_{g0}}T_{g0})\vec{u}_g.\vec{n}\,dS = C_V(\rho_g T_g - \rho_{g,T_{g0}}T_{g0})\int \vec{u}_g.\vec{n}\,dS,$$

i.e. the transport is proportional to the surface integral of the gas velocity. The latter is close to zero, since otherwise this would lead to considerable extraction/injection of gas from/in the closed domain and thus to significant changes in gas density and pressure.

With respect to the energy losses expected due to the back-breakdown (BB) process, we can make an estimation based on the obtained results. The accumulated internal thermal energy in the $\Omega_{95\%P}$ domain at 0.65 ms is about 0.18 mJ. In a first approximation, we can estimate the average power loss due to the BB process as the above number divided by the period of the BB events. Thus if we assume that the period is 0.65 ms, this averaged power loss is $P_{BB} \sim 0.3$ W. If we assume a higher frequency of the BB events and thus a lower period of 0.35 ms, the accumulated internal thermal energy is about 0.1 mJ at 0.35 ms and thus the power loss due to BB events is again

about $P_{BB} \sim 0.3$ W. Apparently the power loss due to the BB process does not vary significantly for the considered conditions and we can assume that the above estimated number is in the right order of magnitude. If we compare this number with the other energy transport mechanisms, the power loss due to BB is more significant than the conductive transport, but it is still very small and insignificant compared to the convective turbulent mechanism, which is in the order of a few W (cf. Figure 12).
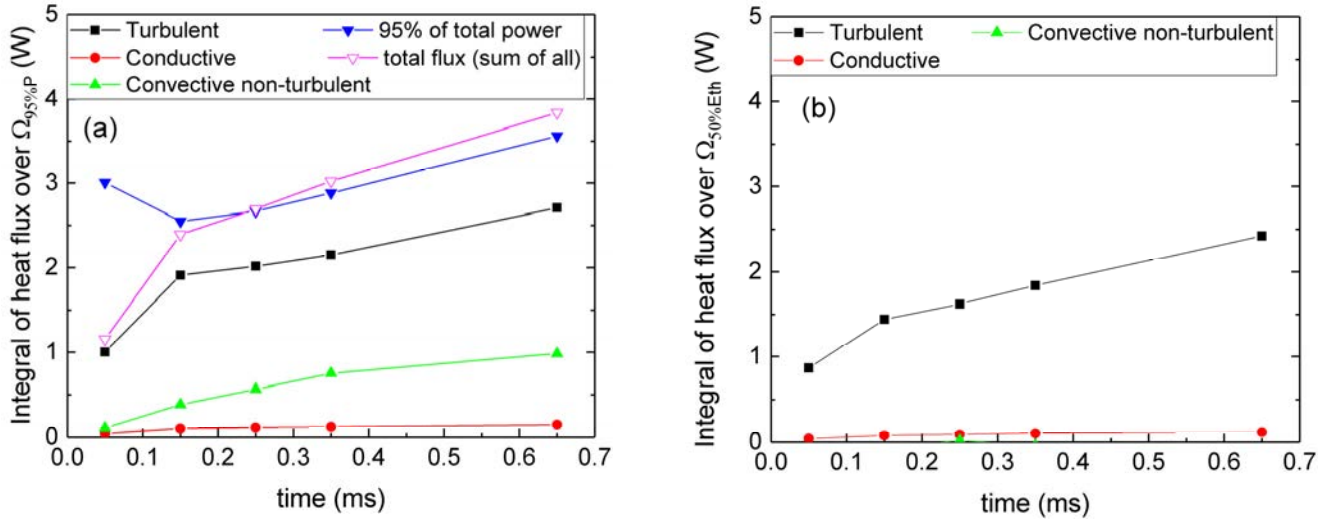

Figure 12. Integrated energy transport fluxes over the surrounding surface of the (a) $\Omega_{95\%P}$ and (b) $\Omega_{50\%Eth}$ domains at various moments in time. In (a) the fluxes are also compared with 95% of the total power deposition, to obtain a better idea on the redistribution of the Joule heating. I_d = 28 mA.

3.2.1 Discharge current I_d = 2.8 mA

At a discharge current of 2.8 mA, the dominant energy transport mechanisms change slightly. Figure 13(a) shows the different transport mechanisms through the surrounding surface of the $\Omega_{95\%P}$ domain. While in the very beginning of the plasma column evolution (0.05 ms) the convective turbulent energy flux still prevails, at later times the convective non-turbulent flux becomes more significant. The reason for that is the slip velocity between the plasma column and the neutral gas, which increases in time (see figure 9). In fact, as we noted before, the plasma column stops moving downstream and starts moving backwards at around 0.32 ms, thus increasing the slip velocity above the gas velocity value. This explains the larger contribution and the peak of the convective non-turbulent energy transport at around 0.5 ms. Later, the discharge converges towards a stationary state, where the convective non-turbulent energy transport remains dominant but comparable to the convective turbulent transport.
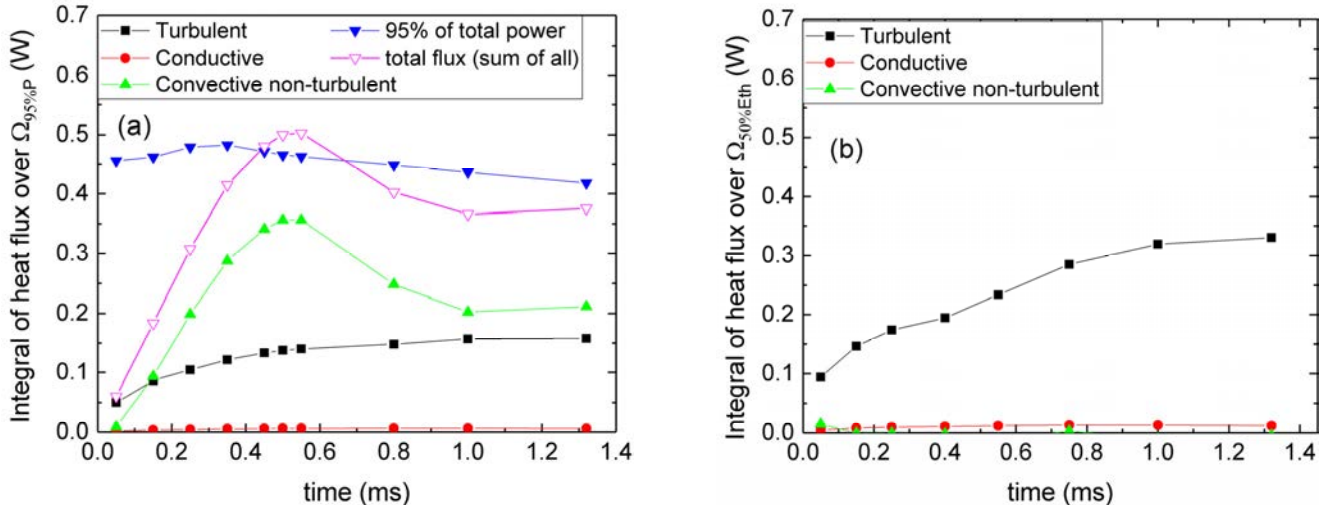

Figure 13. Integrated energy transport fluxes over the surrounding surface of the (a) $\Omega_{95\%P}$ domain and 95% of the total power (blue line), as well as (b) for the $\Omega_{50\%Eth}$ domain. I_d = 2.8 mA.

Note that despite being smaller compared to the convective transport, the turbulent transport here still remains important. It provides more efficient redistribution of the Joule heating in the gas and thus it can prevent the arc contraction during the initial arc formation by keeping the gas temperature low enough so that no contraction can develop.

With respect to the $\Omega_{50\%Eth}$ domain, the results are similar to the 28 mA case - the convective turbulent energy transport is dominant and the convective non-turbulent energy transport is again close to zero.

4. Conclusions

We studied the general discharge behavior and the various heat transport mechanisms in a gliding arc discharge with two diverging electrodes in argon, by means of a 3D numerical model. Specifically, we compared the results at two different discharge currents, i.e., 28 and 2.8 mA, which resulted in significant differences in the discharge properties.

At the higher current, the plasma column is constricted and confined with a relatively small diameter, as a result of thermal instability in the plasma.

At the low current, the gas heating is insufficient to compensate the gas cooling mechanisms and only a slight increase of the gas temperature is observed. Therefore, the discharge is not constricted and it evolves to a diffusive plasma column, of which the shape and distribution is predominantly determined by the electric field distribution, determined by the electrode geometry. This is in contrast to the higher current case, where the contraction is leading to "self-compression" of the plasma column and its shape is determined by the plasma kinetics and its relation to the gas temperature.
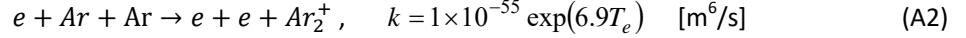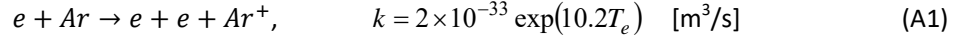
With respect to energy transport in the discharge, our analysis of the energy fluxes through a closed surface surrounding the power deposition zone reveals that the mechanisms are different for the two different discharge regimes with either high or low current. In the higher current case with contraction, the energy transport is mainly controlled by the convective turbulent energy transport, due to a significant forced gas flow. In the case of the lower current and non-constricted discharge, the non-turbulent convective energy transport becomes more significant compared to the turbulent. This is due to the significant slip velocity of the plasma column with respect to the gas. The discharge evolution leads to a static position and no displacement with respect to the electrodes. This means that the slip velocity is high and equal to the gas velocity, thus leading to more significant non-turbulent energy transport compared to turbulent energy transport. In both cases, however, the turbulent transport remains significant and plays an important role. In general, it lowers the average gas temperature in the arc and increases the degree of the plasma thermal non-equilibrium. Even in the lower current case, although smaller, the turbulent transport can change the evolution of the arc towards constricted or non-constricted discharge by lowering the gas temperature to values which do not allow the development of arc contraction.

With respect to applications and specifically for gas treatment, the diffusive low current regime provides a larger processing plasma volume but with much lower excited and charged species densities. This regime allows easier control of the treated gas and of the residence time, since the plasma domain is static and immobile. Moreover, it allows cold gas operation, which might be beneficial for gas treatment applications, because of the stronger thermal non-equilibrium between vibrational temperature and gas temperature. Of course this is not a gliding arc but a glow discharge. In the case of higher current and contracted discharge, it is much more difficult to control the slip velocity and the treated gas volume, since the plasma tends to follow the hot gas regions. However, this regime produces high density plasma, which might give higher efficiency for gas treatment applications. Hence, the most suitable regime will depend on the application and the requirements.

Appendix A. Model description

A.1. *Chemical reactions*

The model applied here is similar to the one used in [20], and in comparison with [23], the model is slightly simplified. It considers five species: Ar, Ar(4s), Ar^+, Ar_2^+ and e. The chemical reactions are the same as the corresponding reactions for these five species in [23]. In order to account approximately for the effect of the Ar(4p) and Ar_2^* species, the model considers two additional effective reactions [20]:

$$e + Ar \rightarrow e + e + Ar^+, \qquad k = 2\times10^{-33}\exp(10.2T_e) \quad [m^3/s] \tag{A1}$$

$$e + Ar + Ar \rightarrow e + e + Ar_2^+, \qquad k = 1\times10^{-55}\exp(6.9T_e) \quad [m^6/s] \tag{A2}$$

Equation (A.1) is used to replace the stepwise ionization process due to Ar(4p), while equation (A.2) replaces the process $e + Ar_2^* \rightarrow e + e + Ar_2^+$, which is considered as the main contributor to the ionization due to Ar_2^*. Note that this approximation produces reasonable results at the considered conditions, but it is not necessarily applicable to other discharge conditions. The complete list of the considered reactions is given in table A1.

Table A1. Chemical reactions used in the model and corresponding reaction rate coefficients

Reaction	Rate coefficient
$e + Ar \rightarrow e + Ar$	BS[a]
$e+Ar \rightarrow e+Ar(4s)$	BS
$e+Ar \rightarrow 2e+Ar^+$	BS
$e+Ar(4s) \rightarrow 2e+Ar^+$	BS
$e+Ar(4s) \rightarrow e+Ar$	BS, DB[b]
$2e+Ar^+ \rightarrow e+Ar$	$k(m^6/s) = 8.75\times10^{-39}T_e^{-2.25}(eV)$
$e+Ar+Ar^+ \rightarrow Ar+Ar$	$k(m^6/s) = 1.5\times10^{-40}(T_g(K)/300)^{-2.5}$
$e+Ar_2^+ \rightarrow Ar+Ar^++e$	$k(m^3/s) = 1.11\times10^{-12}\exp(-(2.94-3(Tg(eV)-0.026))/Te(eV))$
$e+Ar_2^+ \rightarrow Ar(4s)+Ar$	$k(m^3/s) = 1.04\times10^{-12}(\dfrac{300}{Te(K)})^{0.67}\dfrac{1-\exp(-418/Tg(K))}{1-0.31\exp(-418/Tg(K))}$
$Ar(4s)+Ar(4s) \rightarrow e+Ar_2^+$	$k(m^3/s) = 3.15\times10^{-16}(Tg(K)/300)^{-0.5}$
$Ar(4s)+Ar(4s) \rightarrow e+Ar^++Ar$	$k(m^3/s) = 1.62\times10^{-16}(Tg(K))^{0.5}$
$2Ar+Ar^+ \rightarrow Ar_2^++Ar$	$k(m^6/s) = 2.5\times10^{-43}(\dfrac{Tg(K)}{300})^{-1.5}$
$Ar_2^++Ar \rightarrow 2Ar+Ar^+$	$k(m^3/s) = \dfrac{6.06\times10^{-12}}{Tg(K)}\exp(-\dfrac{1.51\times10^4}{Tg(K)})$
$Ar(4s) \rightarrow h\nu+Ar$	$\upsilon_c(s^{-1}) = g_{eff}^c \times 3.145\times10^8$
$e+Ar \rightarrow e+e+Ar^+$	$k(m^3/s) = 2\times10^{-33}\exp(10.2Te(eV))$
$e+Ar+Ar \rightarrow e+e+Ar_2^+$	$k(m^6/s) = 1\times10^{-55}\exp(6.9Te(eV))$

    a.   BS = Boltzmann solver
    b.   DB = Detailed balance
    c. $g_{eff} = (1.15/\pi)(\lambda_{4s}/(6H))$, where $\lambda_{4s} = 105.7$ nm and $H = 1$ mm in our case.

A.2. *Model equations*

The model is based on the quasi-neutral assumption and it consists of the following equations.

The Particle balance equations are

$$\frac{\partial n_s}{\partial t} + \vec{\nabla} \cdot \vec{G}_s + (\vec{u}_g \cdot \vec{\nabla})n_s = S_{c,s} \tag{A3}$$

where n_s is the species density, G_s is the species flux in a reference frame moving with the gas velocity u_g, and $S_{c,s}$ is the collision term representing the net number of particles produced or lost in the volume reactions. The species flux G_s is expressed based on the drift-diffusion approximation, which determines the flux with respect to the gas velocity as:

$$\vec{G}_s = \frac{q_s}{|q_s|} \mu_s n_s \vec{E} - \vec{\nabla} D_s n_s. \tag{A4}$$

In this expression, D_s is the diffusion coefficient and μ_s is the mobility of the corresponding species "s", q_s is their charge, and $\vec{E}$ is the electric field.

The electric field in (A4) is calculated as an ambipolar field, based on the equality of fluxes of positivie (Ar^+, Ar_2^+), and negative species (electrons). The expression used is:

$$\vec{E}_{amb} = \frac{(D_{Ar^+} - D_e)\vec{\nabla}n_{Ar^+} + (D_{Ar_2^+} - D_e)\vec{\nabla}n_{Ar_2^+}}{(\mu_{Ar^+} + \mu_e)n_{Ar^+} + (\mu_{Ar_2^+} + \mu_e)n_{Ar_2^+}} \tag{A5}$$

For the neutral excited species, the flux (A4) is only determined by diffusion, i.e. $\vec{G}_s = -D_s\vec{\nabla}n_s$. The transport coefficients used in the above expressions are the same as in [23]. The argon atom density is considered to be constant. Equation (A3) is solved for the two types of ions and for the excited atoms Ar(4s).

The quasineutrality condition is given by

$$n_e = n_{Ar^+} + n_{Ar_2^+} \tag{A6}$$

The electron energy conservation equation is solved for the averaged electron energy density $n_e\bar{\varepsilon}_e$:

$$\frac{\partial n_e\bar{\varepsilon}_e}{\partial t} + \vec{\nabla} \cdot \vec{G}_{\varepsilon,e} + (\vec{u}_g \cdot \vec{\nabla})n_e\bar{\varepsilon}_e = \sigma\vec{E}_d^2 + n_e\Delta\bar{\varepsilon}_e + Q_{bg} \tag{A7}$$

The electron energy flux $\vec{G}_{\varepsilon,e}$ is

$$\vec{G}_{\varepsilon,e} = -D_{\varepsilon,e}\vec{\nabla}(n_e\bar{\varepsilon}_e) - \mu_{\varepsilon,e}n_e\bar{\varepsilon}_e\vec{E}_{amb} \tag{A8}$$

where $D_{\varepsilon,e}$ is the electron energy diffusion coefficient and $\mu_{\varepsilon,e}$ is the electron energy mobility. The terms at the right hand side represent (i) the Joule heating term ($\sigma\vec{E}_d^2$), where σ is the plasma electric conductivity (see below), (ii) the averaged electron elastic and inelastic collision energy losses ($\Delta\bar{\varepsilon}_e$), and (iii) a constant background power density (Q_{bg}).

Since we employ the quasi-neutrality condition, the electric field due to the external circuit E_d is determined by the current continuity equation:

$$\vec{\nabla} \cdot (-\sigma\vec{\nabla}\phi_d) = 0 \tag{A9}$$

where we have neglected the diffusion terms, present in the full expression of the current conservations. ϕ_d is the electric potential of the external field and $\sigma = |q_e|(\mu_{Ar_2^+}n_{Ar_2^+} + \mu_{Ar^+}n_{Ar^+} + \mu_e n_e)$ is the plasma conductivity, obtained from the sum over the charged species.

The gas thermal balance equation is

$$\rho_g C_p \frac{\partial T_g}{\partial t} + \rho_g C_p \vec{u}_g \cdot \vec{\nabla}T_g - \vec{\nabla} \cdot ((k_g + k_T)\vec{\nabla}T_g) = Q_g \tag{A10}$$

where Q_g is a heat source accounting for the energy transport from the electrons to the heavy particles due to elastic and inelastic collisions. It is expressed as:

$$Q_g = \frac{3m_e m_{Ar}}{(m_e + m_{Ar})^2} n_e n_{Ar} k_{\text{el}} e(T_e - T_g) + \sum_i \Delta\varepsilon_i k_i n_e \, n_i \qquad \text{(A11)}$$

k_{el} is the elastic collision rate coefficient, and $\Delta\varepsilon_i$, k_i and n_i are the inelastic collision energy loss, rate coefficient and collision target density, respectively, for the ith inelastic collision. The electron and gas temperature are expressed in eV in the above equations

Finally, all the equations given above are coupled to the SST RANS model of the gas flow based on [26]. The exact implementation of the model is presented in [27].

ORCID iDs

St Kolev https://orcid.org/0000-0001-7888-7682

A Bogaerts https://orcid.org/0000-0001-9875-6460

References

[1] Fridman A 2008, *Plasma Chemistry* (Cambridge: Cambridge University Press).

[2] Chernichowski A 1994 Gliding Arc. Applications to engineering and environment control *Pure and Appl. Chem.* **6** 1301-1310.

[3] Chun Y, Yang Y and Yoshikawa K 2009 Hydrogen generation from biogas reforming using a gliding arc plasma-catalyst reformer *Catal. Today* **148** 283-9.

[4] Baba T, Takeuchi Y, Stryczewska H and Aoqui S, Study of 6 electrodes gliding arc discharge configuration, 2012 Przegląd Elektrotechniczny **88** 86-8.

[5] Fridman A, Gutsol A, Gangoli S, Ju Y and Ombrello T 2008 Characteristics of Gliding Arc and Its Application in Combustion Enhancement *J. Propulsion Power* **24** 1216-28.

[6] Gallagher M J, Geiger R, Polevich A, Rabinovich A, Gutsol A and Fridman A 2010 On-board plasma-assisted conversion of heavy hydrocarbons into synthesis gas *Fuel* **89** 1187-92.

[7] Nunnally T, Gutsol K, Rabinovich A, Fridman A, Gutsol A and Kemoun A 2011 Dissociation of CO2 in a low current gliding arc plasmatron *J. Phys. D: Appl. Phys.* **44** 274009.

[8] Ramakers M, Trenchev G, Heijkers S, Wang W and Bogaerts A 2017 Gliding arc plasmatron: providing a novel method for CO_2 conversion *ChemSusChem* **10**, 2642-2652

[9] E. Cleiren, S. Heijkers, M. Ramakers and A. Bogaerts 2017 Dry reforming of methane in a gliding arc plasmatron: Towards a better understanding of the plasma chemistry *ChemSusChem* **10** 4025-4036.

[10] Liu J L, Park H W, Chung W J, Ahn W S, Park D W 2016 Simulated biogas oxidative reforming in AC-pulsed gliding arc discharge *Chem Eng J* **285** 243-251

[11] Wang W, Patil B, Heijkers S, Hessel V and Bogaerts A 2017 Nitrogen fixation by gliding arc plasma: Better insight by chemical kinetics modeling *ChemSusChem* **10** 2145-2157.

[12] Patil B, Peeters, F; van Rooij G, Medrano J, Gallucci F, Lang J, Wang Q, Hessel V 2018 Plasma assisted nitrogen oxide production from air: using pulsed powered gliding arc reactor for a containerized plant *AIChE Journal* 2018, 64, 526-537.

[13] Kusano Y et al 2013 Water-cooled non-thermal gliding arc for adhesion improvement of glass-fibre-reinforced polyester *J. Phys. D: Appl. Phys.* **46** 135203.

[14] Li T, Watanabe T, Ochi K, Otsuki K 20013 Liquid waste decomposition by long DC arc under atmospheric pressure *Chemical Engineering Journal* **231** 155–162.

[15] Fridman A, Nester S, Kennedy L A Saveliev A and Mutaf-Yardemci O 1999 Gliding arc gas discharge *Progress in Energy and Combustion Science* **25** 211-231.

[16] Mutaf-Yardimci O, Saveliev A V, Fridman A A and Kennedy L A 2000 Thermal and nonthermal regimes of gliding arc discharge in air flow *J. Appl. Phys.* **87** 1632–1641.

[17] Pellerin S, Richard F, Chapelle J, Cormier J-M, Musiol K 2000 Heat string model of bi-dimensional dc glidarc *J Phys D: Appl Phys* **33** 2407–2419.

[18] Gutsol A F and Gangoli S P, Transverse 2-D Gliding Arc Modeling 2017 *IEEE Trans. Plasma Sci.* **45** 555-564.

[19] Sun S R, Kolev St, Bogaerts A, Investigations of discharge and post-discharge in a gliding arc: a 3D computational study 2017 *Plasma Sources Sci. Technol.* **26** 055017.

[20] Sun S R, Kolev St, Wang H X and Bogaerts A, Coupled gas flow-plasma model for a gliding arc: investigations of the back-breakdown phenomenon and its effect on the gliding arc characteristics 2017 *Plasma Sources Sci. Technol.* **26** 015003.

[21] Kolev St, Sun S R, Trenchev G, Wang W, Wang H X and Bogaerts A, Quasi-Neutral Modeling of Gliding Arc Plasmas 2017 *Plasma Process Polym.* 2017 **14** 1600110.

[22] Trenchev G, Kolev St and Bogaerts A, 3D model of a reverse vortex flow gliding arc reactor 2016 *Plasma Sources Sci. Technol.* **25** 035014.

[23] Kolev St and Bogaerts A, 2D model for a gliding arc discharge 2015 *Plasma Sources Sci. Technol.* **24** 015025.

[24] Tu X, Gallon H J and Whitehead J C 2011 Electrical and optical diagnostics of atmospheric pressure argon gliding arc plasma jet, 30th ICPIG, August 28th – September 2nd 2011, Belfast, Northern Ireland, UK, C10

[25] Tu X, Gallon H J and Whitehead J C 2011 Dynamic behavior of atmospheric argon gliding arc plasma, *IEEE Trans. Plasma Sci.* **39** 2900-2901

[26]. Menter F R, Kuntz M and Langtry R, Ten Years of Industrial Experience with the SST Turbulence Model, in*: Hanjalić K, Nagono Y, Tummers M (Eds.) 2003 Turbulence Heat and Mass Transfer 4 (Begell House Inc., Danbury, USA), pp. 625–632.*

[27] Comsol Multiphysics 5.2 CFD module user guide.

[28] Richard F, Cormier J M, Pellerin S and Chapelle J 1996 Physical study of a gliding arc discharge *J. Appl. Phys.* **79** 2245–2250

[29] Zhu J et al. 2015 Measurements of 3D slip velocities and plasma column lengths of a gliding arc discharge, *Appl. Phys. Lett.*, **106** 044101-1–044101-4.

[30] Wang W, Mei D, Tu X, Bogaerts A 2017 Gliding arc plasma for CO2 conversion: Better insights by a combined experimental and modelling approach *Chemical Engineering Journal* **330** 11–25

[31] Wang W, Berthelot A, Kolev St, Tu X and Bogaerts A CO2 conversion in a gliding arc plasma: 1D cylindrical discharge model 2016 *Plasma Sources Sci. Technol.* 25 065012

[32] Staack D, Farouk B, Gutsol A and Fridman A 2008 DC normal glow discharges in atmospheric pressure atomic and molecular gases *Plasma Sources Sci. Technol.* **17** 025013

[33] Arkhipenko V I, Kirillov A A, Safronau Y A and Simonchika L V 2010 DC atmospheric pressure glow microdischarges in the current range from microamps up to amperes *Eur. Phys. J. D* **60** 455-463[34] Kolev St, Bogaerts A, Similarities and differences between gliding glow and gliding arc discharges 2015 *Plasma Sources Sci. Technol.* **24** 065023

[35] Golubovskii Yu B, Nekuchaev V, Gorchakov S and Uhrlandt D 2011 Contraction of the positive column of discharges in noble gases *Plasma Sources Sci. Technol.* **20** 053002

[36] Ramakers M, Trenchev G, Heijkers S, Wang W, and Bogaerts A 2017 Gliding Arc Plasmatron: Providing an Alternative Method for Carbon Dioxide Conversion *ChemSusChem* **10** 1 – 12

[37] Sun SR, Wang H X, Mei D H, Tu X, Bogaerts A, CO_2 conversion in a gliding arc plasma: Performance improvement based on chemical reaction modeling 2017 *Journal of CO2 Utilization* **17** 220–234.

[38] Berthelot A and Bogaerts A 2017 Modeling of CO2 Splitting in a Microwave Plasma: How to Improve the Conversion and Energy Efficiency *J. Phys. Chem. C* **121** 8236–8251

[39] Trenchev G,Kolev St, Wang W, Ramakers M, and Bogaerts A 2017 CO2 Conversion in a Gliding Arc Plasmatron: Multidimensional Modeling for Improved Efficiency *J. Phys. Chem. C* **121** 24470–24479

[40] Poinsot T and Veynante D. 2005 *Theoretical and Numerical Combustion*, 2nd ed. (R.T. Edwards Inc, Philadelphia, USA) p. 3.

[41] Kessler D and Robert G 1999 *Momentum, Heat, and Mass Transfer Fundamentals* (Lmarcel Dekker Inc. New York Basel) p. 517